Engineering Analysis with Boundary Elements 108 (2019) 158–167

Contents lists available at ScienceDirect

Engineering Analysis with Boundary Elements

journal homepage: www.elsevier.com/locate/enganabound

Spherical porous particle drying using BEM approach

T. Gomboc*, J. Iljaž, J. Ravnik, M. Hriberšek

Faculty of Mechanical Engineering, University of Maribor Smetanova 17, SI-2000 Maribor, Slovenia

ARTICLE INFO

Keywords:
Spherical particle
Porous media
Boundary Element Method
Laplace fundamental solution
Elliptic fundamental solution
Spray drying
1D approach

ABSTRACT

The paper covers a porous particle drying problem, which can be divided into two or three stages. The first stage is drying of surface moisture, the second stage is drying inside the particle, and the third, one which is relevant only to hygroscopic material, represents the change of particle moisture due to the change of environmental moisture. The second stage is the most relevant for the porous materials, and is, therefore, covered in more detail in this paper, with the main focus on the heat transfer inside the particle which affects the drying kinetics. The heat transfer problem inside the spherical particle has been solved using BEM, by transforming a 3D problem into a quasi 1D case by assuming uniform boundary conditions all around the particle, resulting in the solution depending only on the radial direction. The solution of the heat transfer needs to be calculated accurately as it directly affects the evaporation rate of the liquid on the interface between the dry crust and the wet core, which dictates the drying speed and affects the drying time. An in-depth analysis of space and time discretisation was performed on a typical spray drying example, where it is shown that a choice of a correct time step is cruicial for achieving good computational accuracy of the drying kinetics. The proposed numerical approach has also been tested on various drying conditions, with changing the particle size and the temperature of the drying gas, which have a largest effect on the drying kinetics. Finally, an analysis of the computed drying times is made as this is the most important parameter from the practical point of view, especially when designing the drying chambers.

1. Introduction

Modelling of the drying process presents a challenge in research as well as in the industrial environment. A special challenge is numerical modelling of drying of porous particles. Most of the commercial CFD (Computer Fluid Dynamic) codes for particles drying treat all the moisture as a surface moisture using one-stage models, where only particle surface moisture is removed. However, because porous particles contain also the fluid phase (moisture), more complex models have to be used, and the one-stage drying model is not sufficient. One of such processes, where multi-stage drying models are more suitable to use, is the spray drying process. The one stage drying models are suitable for solid, non-porous materials drying, where the interior does not contain moisture.

In spray drying, the solution to be dried is typically atomized by a spray nozzle, located in the drying cyclone, which produces slurry droplets with a size between 50 μm and 300 μm. Depending on the spray dryer size, from a hundred thousand to a few hundred thousand particles are typically present in the system. Usually hot air is used as the drying medium. Drying of small particles with hot air or any different drying medium was studied in several works. A simplified Reaction Engineering Approach (REA) was developed by Fu et al. [1], for simulating three different stages in drying kinetics, where a fractional coefficient was introduced to model kinetics of vapour density at the surface of a droplet during all drying stages, hence, determining the convective flux of moisture from the outer surface. Based on the similar idea, Langrish and Kockel [2] developed a drying kinetics model where a typical material characteristic drying curve in the case of milk powder was used. A physically more complex model, where a two stage approach for modelling heat, mass and momentum transfer in a coal-water slurry droplet, was developed by Levi-Hevroni et al. [3]. A simple heat balance was used to determine the average temperatures of the wet core and the dry crust. A numerical solution of the balance equations was obtained using Gear's method [4], where mass transfer through the dry crust was modelled with Stefan diffusion. A published two stage model by Mezhericher et al. [5] was extended to the solution of Partial Differential Equation (PDE), to solve the temperature profile within the particle. In Mezhericher et al. [6], a diffusion based model, for predicting the mass transfer rate through the dry crust, was replaced by the PDE based diffusion equation for the vapour fraction in the dry crust, where the capillary pore was treated as a straight cylindrical tube. A fully implicit finite difference scheme was applied for solving the resulting PDE. A new model based on population balance theory was presented by Handscomb et al. [7]. The model is able to give details on morphology evolution for multi-component mixtures within the drying particle. In Sagadin et al. [8], a two stage model was presented for drying of porous particles. The temperature profile within the particle was solved through the PDE and a Stefan diffusion model was used for mass transfer rate through the dry crust. A sphere shaped droplet with spherical symmetry was used,

* Corresponding author.
E-mail address: timi.gomboc@um.si (T. Gomboc).

https://doi.org/10.1016/j.enganabound.2019.07.019
Received 29 March 2019; Received in revised form 8 July 2019; Accepted 29 July 2019

which reduced all the PDEs in the final model to a single spatial dimension. The presented model was upgraded to a three stage drying model for zeolite-water suspension droplet drying in Sagadin et al. [9], where additionally the adsorption characteristics of the zeolite were taken into account. The Finite Difference Method was applied for the solution of the heat transfer problem in the interior of the particle. The developed three stage porous particle drying models are suitable for the implementation in the context of Computational Fluid Dynamics (CFD), especially for the case of Lagrangian particle tracking (Langrish [10], Ravnik et al. [11,12], Fletcher et al. [13]).

For solving mathematical models derived for porous particle drying, usually Finite Difference (FD) method was used [6,8,9]. However, in this paper, we are proposing the BEM (Boundary Element Method) for the solution of governing equations in the three-stage mathematical model for porous particle drying [9]. BEM has been proven on various linear and non-linear problems, from diffusion problems of heat and mass transfer, freeze-drying, bioheat problems, fluid flow etc. [14–16]. Drying of porous particles is divided into three stages. In the first stage the surface moisture is removed, while, in the second stage, the drying inside the porous particle takes place. At this stage, the particle is divided into two regions (the outer region which is already dry and the inner region which is still wet). Dry crust and wet core are separated by a drying front, where the moisture evaporation takes place. Mass transfer through the particle interior is modelled using the Stefan diffusion model. After the moisture in the porous particle interior is removed, the process of desorption now becomes the main mechanism of drying, which characterises the third stage of drying. A mathematical model of the first and third drying stages contain only an accumulation term leading to ordinary differential equations, which can be solved by using an iterative method (Runge–Kutta method, Euler method). The heat transfer problem in the particle interior has to be solved in the second drying stage, where the mechanism of diffusion governs the physics of the problem. In the present paper, the heat transfer problem was solved using the BEM, with the particle modelled as a small sphere with uniform boundary conditions prescribed in the exterior of the particle, leading to the heat transfer problem solved only in the radial direction.

The paper is organised as follows. Section 2 describes the mathematical model of the second drying stage. Description of the BEM implementation with fundamental solution and numerical discretisation of governing equations are presented in Section 3. Computational examples are presented in Section 4, while results and discussion are presented in Section 5. The paper ends with the Conclusion and Acknowledgments in Section 6.

2. Mathematical model

A three-stage model should be used to describe porous particles drying. However, in this paper, we are covering just the modelling of the second stage, which is governed by the heat transfer inside the particle and the Stefan diffusion through the dried part of the particle accounting for the mass transfer. As already mentioned, the governing equations for the first and the third drying stages are Differential Equations with respect only to time, and can be solved by standard iterative solvers based on Euler or Runge–Kutta algorithms, and are of no interest here.

During the second stage, drying inside the particle takes place, where the moisture is evaporated and transferred to the outer surface of the particle by means of the Stefan diffusion. Therefore, the particle can be divided into two regions during the second stage - the dry and wet regions as shown in the Fig. 1. The dry region is usually called a dry crust, and the the wet region a wet core. These two regions are separated with the interface area where evaporation takes place. During the drying stage, the interface area is changing as the wet core decreases in size until there is no wet region inside the particle. Therefore, to solve the second stage, we have to solve the heat transfer inside the particle, which affects the drying speed, taking into account the evaporation on the interface area.

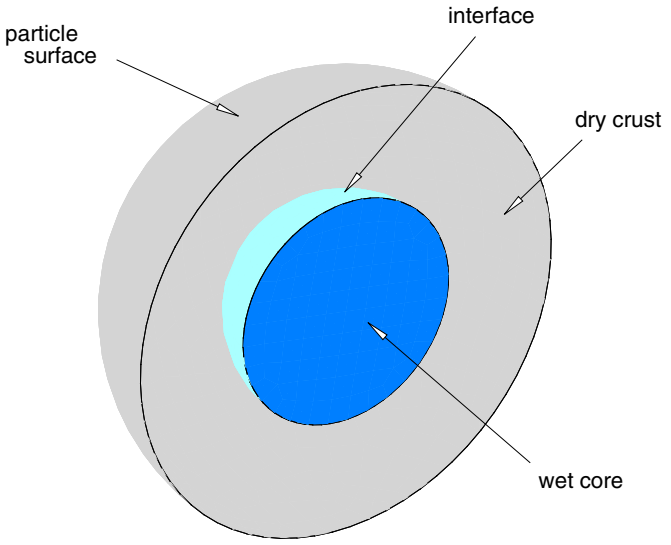

Fig. 1. Schematic presentation of the drying particle through the second drying stage.

Heat transfer inside the wet core and the dry crust can be described by the conservation of energy as

$$\rho_i c_i \frac{\partial T_i}{\partial t} = \vec{\nabla} \cdot \left(\lambda_i \vec{\nabla} T_i \right), \tag{1}$$

where $\vec{\nabla}$ represents nabla operator, c effective specific heat capacity, λ effective heat conductivity, T temperature, t time and index $i = w, d$ denotes wet or dry region.

To solve the unsteady heat transfer through the dry and wet regions we also have to impose boundary and interface conditions. Due to the particle spherical shape, we introduce a spherical coordinate system $\vec{r} = \vec{r}(r, \varphi, \theta)$ for simpler annotation. Heating or cooling of a particle on the outer surface is described with Robin boundary condition as

$$q = -\lambda_d \vec{\nabla} T_d \cdot \vec{n} = \alpha (T_g - T_d), \quad r = R_p, \quad 0 \le \varphi \le 2\pi, \quad -\pi \le \theta \le \pi, \tag{2}$$

where q represents the heat flux, T_d the temperature of the dry crust, T_g is the temperature of the drying gas far away from the particle, α is the heat transfer coefficient, λ_d the effective heat conductivity of the dry region, $\vec{n}$ is a normal vector of the surface, and R_p the radius of the particle. At the interface we impose a compatibility condition for the temperature as

$$T_w = T_d, \qquad r = R_i, \quad 0 \le \varphi \le 2\pi, \quad -\pi \le \theta \le \pi, \tag{3}$$

where T_w represents the temperature of the wet core, R_i is the interface radius, and equilibrium conditions, where evaporation of the moisture is included, as

$$\lambda_d \frac{\partial T_d}{\partial r} = \lambda_w \frac{\partial T_w}{\partial r} + h \frac{\dot{m}_{f,i}}{A_i} \quad r = R_i, \quad 0 \le \varphi \le 2\pi, \quad -\pi \le \theta \le \pi \tag{4}$$

where λ_w represents the effective thermal conductivity of the wet core, h is the specific heat of evaporation, A_i is the interface surface area, and $\dot{m}_{f,i}$ the fluid vapour mass flow rate at the interface. Because the boundary conditions on the particle surface (2) are uniform in all directions and the particle is treated as homogeneous, the drying rate will also be the same in all directions. Therefore, heat transfer does not depend on angles, but only on the radial direction and the problem can be treated as quasi 1D problem.

As stated, mass transfer of vapour from the interface area to the particle surface through the dried crust is solved by using the solution of the Stefan diffusion through a porous material under the assumption of

cylindrical inner channels, which is described with the equation [5]

$$\dot{m}_{f,i} = -\frac{8\pi\varepsilon^{\beta} D_{f,d} M_f p_g}{\kappa\left(\bar{T}_d + \bar{T}_w\right)} \frac{R_p R_i}{R_p - R_i} ln\left[\frac{p_g - p_{f,i}}{p_g - \left(\frac{\kappa}{4\pi M_f \alpha_m R_p^2}\dot{m}_{f,i} + \frac{p_{f,\infty}}{T_g}\right)T_i}\right], \quad (5)$$

where ε represents the porosity of the particle, β the power coefficient, M_f the fluid molecular weight, κ the universal gas constant, p_g the drying gas pressure, $D_{f,d}$ the vapour diffusion coefficient in the dry crust, $\bar{T}_d$ and $\bar{T}_w$ are the average temperature of the dry crust and the wet core, respectively, T_i represents the temperature at the wet core-dry crust interface, $p_{f,i}$ is the saturation pressure of vapour on interface while $p_{f,\infty}$ represent the partial pressure of the vapour in the drying gas and α_m the mass transfer coefficient. The saturation pressure of the vapour depends on the temperature and is calculated from the model [9]:

$$p_{f,i} = \frac{e^{a_1 + a_2 T_i \frac{a_3}{T_i}}}{T_i^{a_4}}, \quad (6)$$

while other parameters in the Eq. (5) are kept constant. Variables a_1, a_2, a_3, and a_4 in the Eq. (6) are constants. As can be seen, Eq. (5) for calculation of mass flow rate for the evaporated fluid at the interface is non-linear and has to be solved using an iterative approach.

The change of the wet core volume is calculated using the conservation of mass written for the fluid, assuming that the wet core has a spherical shape, as

$$\frac{\partial R_i}{\partial t} = -\frac{1}{\varepsilon \rho_f 4\pi R_i^2}\dot{m}_{f,i}, \quad (7)$$

where ρ_f represents the fluid density.

The heat transfer problem described with Eq. (1), written for dry and wet regions, together with boundary and interface conditions (2)–(4) has been solved using the BEM method that will be described in the next section, while Eq. (5) has been solved using an iterative solver and Eq. (7) and the classical Euler algorithm.

As can be seen from the described model for the second drying stage, we are dealing with a transient problem that is terminated when the radius of the interface reaches zero, $R_i = 0$, while for the starting point, we prescribed a constant temperature of the particle T_0 for both regions, and the starting radius for the interface was set to $R_{i,0} = 0.99R_p$.

3. Boundary element method

The BEM was used to solve the heat transfer process inside the porous particle described with Eq. (1) and boundary and interface conditions (2)–(4). The main reason for choosing this method is its advanced treatment of boundary conditions, especially the treatment of flux or normal derivative of the field function, which is incorporated directly in the formulation without any additional approximation, and, therefore, increases the accuracy of the numerical solution. The numerical formulation used to solve the quasi 1D heat transfer problem for 3D spherical computational domain presented in this paper is based on the elliptic fundamental solution. In this section a short description of BEM formulation will be presented, treating the problem as 3D that can be transformed to a quasi 1D problem in a radial direction due to the spherical shape of the computational domain, and assumption of the uniform boundary conditions.

Heat transfer through the porous particle for wet and dry regions described by Eq. (1), has been treated as a Poisson equation, for which the BEM formulation is made. Poisson equation can in general be written as

$$\vec{\nabla}^2 u(\vec{r}) = b(\vec{r}), \quad (8)$$

where $\vec{\nabla}^2$ represents the Laplace operator, $u(\vec{r})$ is a field function, which, in our case, represents temperature, $b(\vec{r})$ is a non-homogenous term on the right hand side, and $\vec{r} = \vec{r}(r, \varphi, \theta)$ is an arbitrary spatial vector. Introducing the integral form of Green's second identity for Poisson equation, we can write it as:

$$c(\vec{\xi})u(\vec{\xi}) + \int_\Gamma u(\vec{R})q^*(\vec{\xi}, \vec{R})d\Gamma + \int_\Omega b(\vec{r})u^*(\vec{\xi}, \vec{r})d\Omega = \int_\Gamma q(\vec{R})u^*(\vec{\xi}, \vec{R})d\Gamma \quad (9)$$

where Ω represents the computational domain, Γ is its boundary, $\vec{\xi} = \vec{\xi}(r, \varphi, \theta)$ is the position of the source point, $\vec{R} = \vec{R}(r, \varphi, \theta)$ is the spatial vector of the boundary, $\vec{q} = \vec{\nabla}u \cdot \vec{n}$ represents the normal derivative of the field function, $c(\vec{\xi})$ is the free coefficient that depends on the position of the source point, and u^* and q^* are the fundamental solution and its normal derivative, respectively. An elliptical fundamental solution for 3D is defined as

$$u^*(\vec{\xi}, \vec{r}) = \frac{1}{4\pi d(\vec{\xi}, \vec{r})}, \quad (10)$$

where $d(\vec{\xi}, \vec{r})$ represents the distance from the source and the field point:

$$d(\vec{\xi}, \vec{r}) = \sqrt{r_\xi^2 + r_p^2 - 2r_\xi r_p \cos(\theta_\xi - \theta_p) - 2r_\xi r_p \sin(\theta_\xi)\sin(\theta_p)\left[\cos(\varphi_\xi - \varphi_p) - 1\right]}, \quad (11)$$

where the source point is defined by coordinates $\vec{\xi} = \vec{\xi}(r_\xi, \varphi_\xi, \theta_\xi)$, and the field point by $\vec{r} = \vec{r}(r_p, \varphi_p, \theta_p)$. The normal derivative of the fundamental solution is defined by the equation:

$$q^*(\vec{\xi}, \vec{R}) = \vec{\nabla}u(\vec{\xi}, \vec{R}) \cdot \vec{n} = \frac{\partial u^*(\vec{\xi}, \vec{R})}{\partial r} n_r + \frac{1}{r \sin(\theta)} \frac{\partial u^*(\vec{\xi}, \vec{R})}{\partial \varphi} n_\varphi + \frac{1}{r} \frac{\partial u^*(\vec{\xi}, \vec{R})}{\partial \theta} n_\theta, \quad (12)$$

where surface normal vector $\vec{n}$ is defined as $\vec{n} = \vec{n}(n_r, n_\varphi, n_\theta)$.

Because the computational domain for the wet core or dry crust is always presented by a sphere or hollow sphere, therefore, the free coefficient $c(\vec{\xi})$, which depends on the position of the source point, can be:

$$c(\vec{\xi}) = 1, \quad \vec{\xi} \in \Omega,$$
$$c(\vec{\xi}) = 0.5, \quad \vec{\xi} \in \Gamma. \quad (13)$$

Assuming a constant interpolation for the field function $u(\vec{R})$ and normal derivative $q(\vec{R})$ on the spherical surface or boundary of the wet or dry regions a surface integral in Eq. (9) can be evaluated analytically as

$$\int_{\Gamma_j} q^*(\vec{\xi}, \vec{R}_j)d\Gamma_j = 0, \quad \int_{\Gamma_j} u^*(\vec{\xi}, \vec{R}_j)d\Gamma_j = R_j^2/r_\xi, \quad r_\xi > R_j \quad (14)$$

where r_ξ represents the radial coordinate of the source point $\vec{\xi}$, and index j the spherical surface Γ_j with radius R_j. For the case when the position of the source point is inside the spherical surface, the surface integrals are:

$$\int_{\Gamma_j} q^*(\vec{\xi}, \vec{R}_j)d\Gamma_j = -1, \quad \int_{\Gamma_j} u^*(\vec{\xi}, \vec{R}_j)d\Gamma_j = R_j, \quad r_\xi < R_j \quad (15)$$

and when the source point is on the integration surface:

$$\int_{\Gamma_j} q^*(\vec{\xi}, \vec{R}_j)d\Gamma_j = -0.5, \quad \int_{\Gamma_j} u^*(\vec{\xi}, \vec{R}_j)d\Gamma_j = R_j, \quad r_\xi = R_j. \quad (16)$$

However, the domain integral in Eq. (9) can not be solved analytically, and numerical integration has to be used. Due to the uniform boundary conditions on the spherical surface, the field function depends only on the radial distance, $u(\vec{r}) = u(r_p)$, and, therefore, only discretisation of computational geometry is needed in the radial direction. Domain discretisation can, therefore, be represented by a 1D numerical mesh composed of linear elements. For the approximation of the non-homogeneous part $b(\vec{r})$, we used the quadratic interpolation function inside the domain, with the 3 node linear element. Using domain discretisation, by dividing domain Ω into n sub-domains Ω_e and by using

the quadratic interpolation inside Ω_e, the domain integral can be calculated as:

$$\int_{\Omega} bu^*(\vec{\xi},\vec{r})d\Omega = \sum_{e=1}^{n}\sum_{k=1}^{3} b_k \int_{\Omega_e} \Phi_{k,e}u^*(\vec{\xi},\vec{r})d\Omega_e, \tag{17}$$

where index e represents the element or sub-domain, k the interpolation or node number of the element, n is the number of elements, and Φ the interpolation function. Therefore, b_k represents the value of non-homogeneous terms in node k and $\Phi_{k,e}$ is the interpolation function for node k of element e. The sub-domain integral in Eq. (17) was solved numerically using Simpson's rule, where integration in the spherical coordinates has been used, as

$$\begin{aligned}\int_{\Omega_e} \Phi_{k,e}u^*(\vec{\xi},\vec{r})d\Omega_e &= \int_{R_{e1}}^{R_{e2}}\int_{0}^{2\pi}\int_{-\pi}^{\pi} \Phi_{k,e}u^*(\vec{\xi},\vec{r})r^2\sin(\theta)drd\varphi d\theta \\ &= \sum_{i=1}^{n_r}\sum_{j=1}^{n_\varphi}\sum_{k=1}^{n_\theta} \omega\Phi_{k,e}u^*(r,\varphi,\theta)J\Delta r\Delta\varphi\Delta\theta,\end{aligned} \tag{18}$$

where R_{e1} and R_{e1} represent the radius of the boundary of subdomain Ω_e or element e, n_r, n_φ and n_θ represent the number of subdivisions in the radial and both angular directions, $\Delta r = (R_{e2} - R_{e1})/n_r$ represents the integral discretisation in the radial direction, $\Delta\varphi = 2\pi/n_\varphi$ discretisation of subdomain Ω_e along the angle φ, $\Delta\theta = 2\pi/n_\theta$ discretisation along the θ angle, J represents the Jacobian, which is $J = r^2\sin(\theta)$, and ω are the integration weights.

When the source point $\vec{\xi}$ is set in every computational node defined by the numerical mesh, we can write the system of linear equations as:

$$[H]\{u\} = [G]\{q\} + [S]\{b\}, \tag{19}$$

where $[H]$, $[G]$ and $[S]$ represent matrices, $\{u\}$ represents the vector of field variable u at computational nodes, $\{q\}$ represents the vector of flux at the computational nodes, and $\{b\}$ the vector of non-homogenous term b in computational nodes. Elements of the matrices $[H]$, $[G]$ and $[S]$ are according to Eqs. (14)–(17):

$$\begin{aligned} h_{i,j} &= \int_{\Gamma_j} q^*(\vec{\xi}_i,\vec{R}_j)d\Gamma_j, \quad g_{i,j} = \int_{\Gamma_j} u^*(\vec{\xi}_i,\vec{R}_j)d\Gamma_j, \\ s^e_{i,j} &= \int_{\Omega_e} \Phi_{j,e}u^*(\vec{\xi}_i,\vec{r})d\Omega_e. \end{aligned} \tag{20}$$

The derived system of Eqs. (19) solves a Poisson equation (8) for the field function u in the radial direction, and, therefore, it is solving a diffusion problem in quasi 1D, with numerical mesh needed only in the radial direction.

Now, we can apply the derived formulation on the case of the heat transfer equation (1), which, for constant material properties, can be rewritten in the Poison form as

$$\vec{\nabla}^2 T_i = \frac{1}{a_i}\cdot\frac{\partial T_i}{\partial t} \tag{21}$$

where $a_i = \lambda_i/(\rho_i c_i)$ represents thermal diffusivity. To approximate the time derivative in Eq. (21), we used an first order finite difference scheme as

$$\frac{\partial T_i}{\partial t} \approx \frac{T_i^t - T_i^{t-1}}{\Delta t} \tag{22}$$

where superscript t and $t-1$ represent different time steps, and Δt is the time difference between two time steps. Including the approximation (22) into Eq. (21) and using a fully implicit scheme ($T_i = T_i^t$, $q_i = q_i^t$) the global system of Eq. (19) can be rewritten as:

$$\left([H] - \frac{1}{a\cdot\Delta t}[S]\right)\{T_i^t\} = [G]\{q_i^t\} - \frac{1}{a\cdot\Delta t}[S]\{T_i^{t-1}\}. \tag{23}$$

Writing a system of Eq. (23) for the wet and dry regions, imposing the interface and boundary conditions, a global linear system of equations is obtained, which has to be solved only once in each time step using a standard solver. The result of the heat transfer equation is the radial temperature distribution inside the porous particle that affects the drying kinetic described by Eqs. (5) and (7).

Eq. (5) for the mass flow rate at the interface has been solved using a classical iteration method, while for Eq. (7), the Euler algorithm has been used, which can be written as

$$R_i^{t+1} = R_i^t - \frac{\dot{m}^t_{f,i}}{\varepsilon\rho_f 4\pi(R_i^t)^2}, \tag{24}$$

where superscript $t+1$ and t represent the next and current time steps, respectively.

Because of the changing interface between the wet and dry regions, the computational domain has to follow the movement of the interface by a simple interface tracking procedure, and the system of Eq. (23) has to be therefore re-evaluated at each time step. The system of Eqs. (1), (5) and (7), together with the interface conditions (3) and (4), is non-linear, and has been solved assuming constant mass flow rate and interface radius inside each time step. The algorithm for solving the particle second drying stage inside each time step can therefore be written as:

ALGORITHM

1. Solving heat transfer inside the particle:
   - Calculating the matrices $[H]$, $[G]$ and $[S]$ defined by Eq. (20) for wet and dry region,
   - imposing the compatibility and equilibrium interface conditions (3) and (4),
   - applying Robin boundary condition (2),
   - solving temperature field $T = T(r)$ inside the particle,
   - calculation of average temperature $\bar{T}_w$ and $\bar{T}_d$.
2. Calculating mass flow rate $\dot{m}_{f,i}$ at the interface by Eq. (5),
3. Calculating the new interface radius R_i by algorithm (24),
4. Move the computational mesh and data interpolation on the new mesh.

4. Computational examples

The paper presents a development of the numerical model for porous particle drying based on the BEM solution of the heat transfer inside the particle. In this section, we will present several computational examples to evaluate the numerical model, and show how the space and time discretisation affects the solution of the second drying stage. A special attention will be devoted to reducing the numerical error to a minimum to achieve an accurate numerical solution and to reducing the drying time, which becomes important when the derived model is used in the context of CFD.

In the literature, no real benchmark tests for the second drying stage could be found, therefore, we had to set up our own test examples by varying the particle diameter and temperature of the drying gas, which affect the drying kinetics at most. The test example set-ups are based on the drying of Zeolite 4*A*-water suspension by means of hot drying air, where the moisture inside the Zeolite is water, case which was validated in [9]. Depending on the nozzle for particle formation, particle sizes can vary from a hundred to a few hundred micro meters. Therefore, for our mesh validation, two different sizes of particles were used; $D_p = 2R_p = 100$ μm and 300 μm, while, for the drying temperature, $T_g = 100$ °C and 300 °C were used, where the latter one represents the conditions where the evaporation process is very intense. Depending on the particle size and the drying temperature, different test examples were defined, while the other model parameters and material properties have been kept constant for all test examples. The most important parameter for practical use is particle drying time. For this reason the analysis of the influence of the particle diameter, the particle-drying air relative velocity and drying temperature, on the drying time was done. The drying gas temperature has been varied in the range between 100 °C and 300 °C with the step 20 °C the particle diameter in the range between 100 μm and 300 μm with the step 20 μm, and the particle relative velocity in the range between 0.4 m/s and 1.4 m/s with the step

Table 1
Material properties for Zeolite 4A, wet core and water.

	Density (kg/m^3)	Specific heat (J/kg K)	Thermal conduc. (W/m K)
Zeolite 4A	1270	850	0.2
Wet core	1590	4185	0.6
Water	983	1926 (vapour)	–

0.1 m/s, which presented the basis for execution of a full factorial DOE (Design of Experiment).

The used material properties for water, Zeolite 4*A* and its wet core are presented in the Table 1. For the material properties for the dry crust we used the Zeolite 4*A* properties, while, for the wet core, the effective material properties were calculated based on Zeolite 4*A* porosity, which is $\varepsilon = 0.26$, and water.

In the numerical simulations the following constant values were used: heat transfer coefficient, determined on the basis of the Nusselt number and the particle relative velocity, was $\alpha = 950.1$ W/m^{2}K^1, mass transfer coefficient $\alpha_m = 0.32$ m / s, partial pressure of the vapour in the drying gas $p_{f,\infty} = 3156.5$ Pa, universal gas constant $\kappa = 18.0153$ kg/kmol and vapor diffusion coefficient in the dry crust $D_{f,d} = 0.00009$ m^2/s. Value of parameters in the Eq. (6) were: $a_1 = 77.345$, $a_2 = 0.0075$, $a_3 = 7235$ and $a_4 = 8.2$.

5. Results and discussion

In this section, the simulation results of the porous particle drying are presented for the different examples discussed in the previous section. At the beginning, the space and time discretisation analysis has been done to determine the appropriate mesh size and time step value in order to achieve adequate numerical accuracy of the results. After that, the results for different examples are presented, followed by a dis-

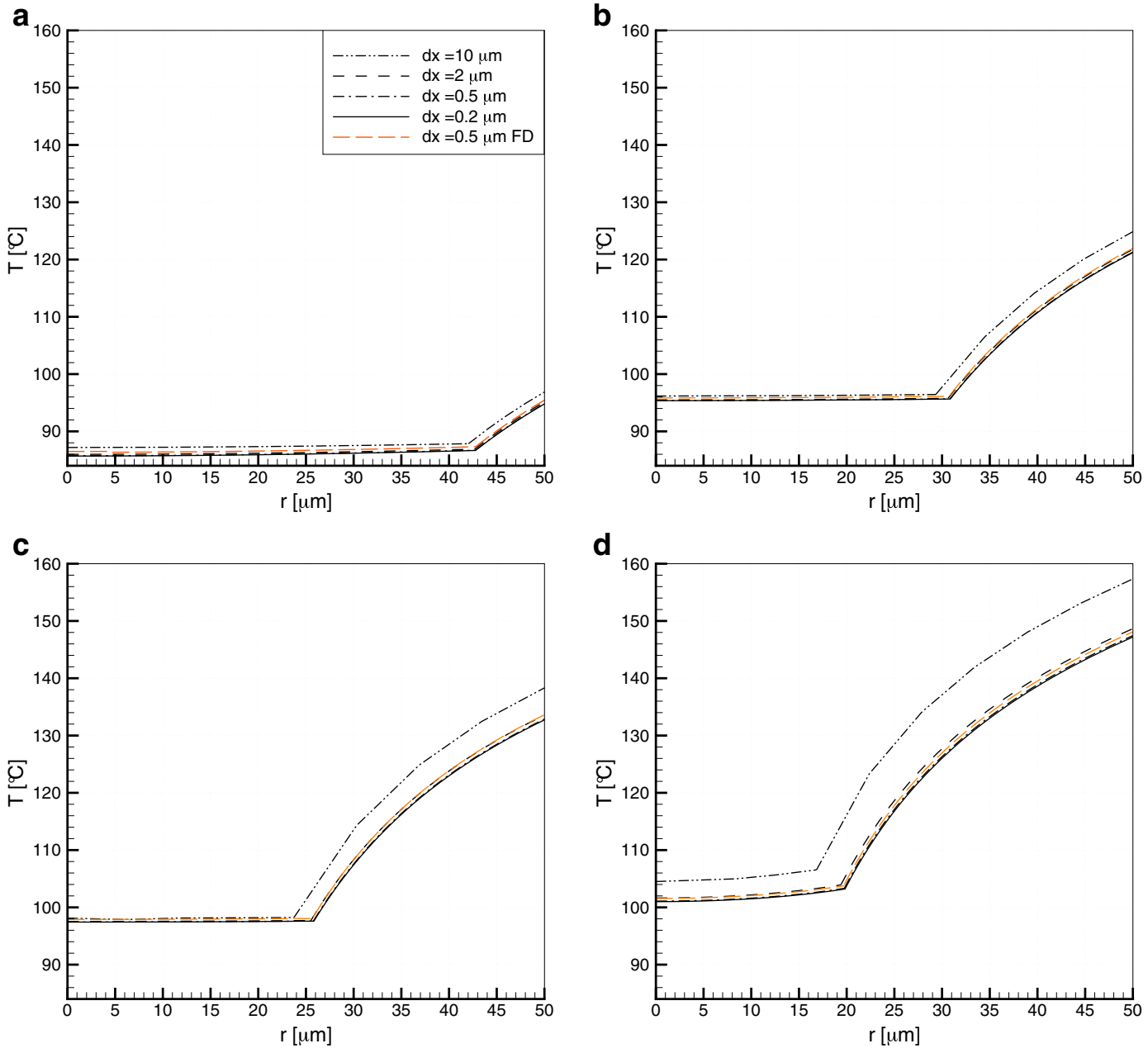

Fig. 2. Particle temperature profile through the particle drying, for different mesh sizes at following times: (a) 0.03 s, (b) 0.05 s, (c) 0.06 s and (d) 0.07 s.

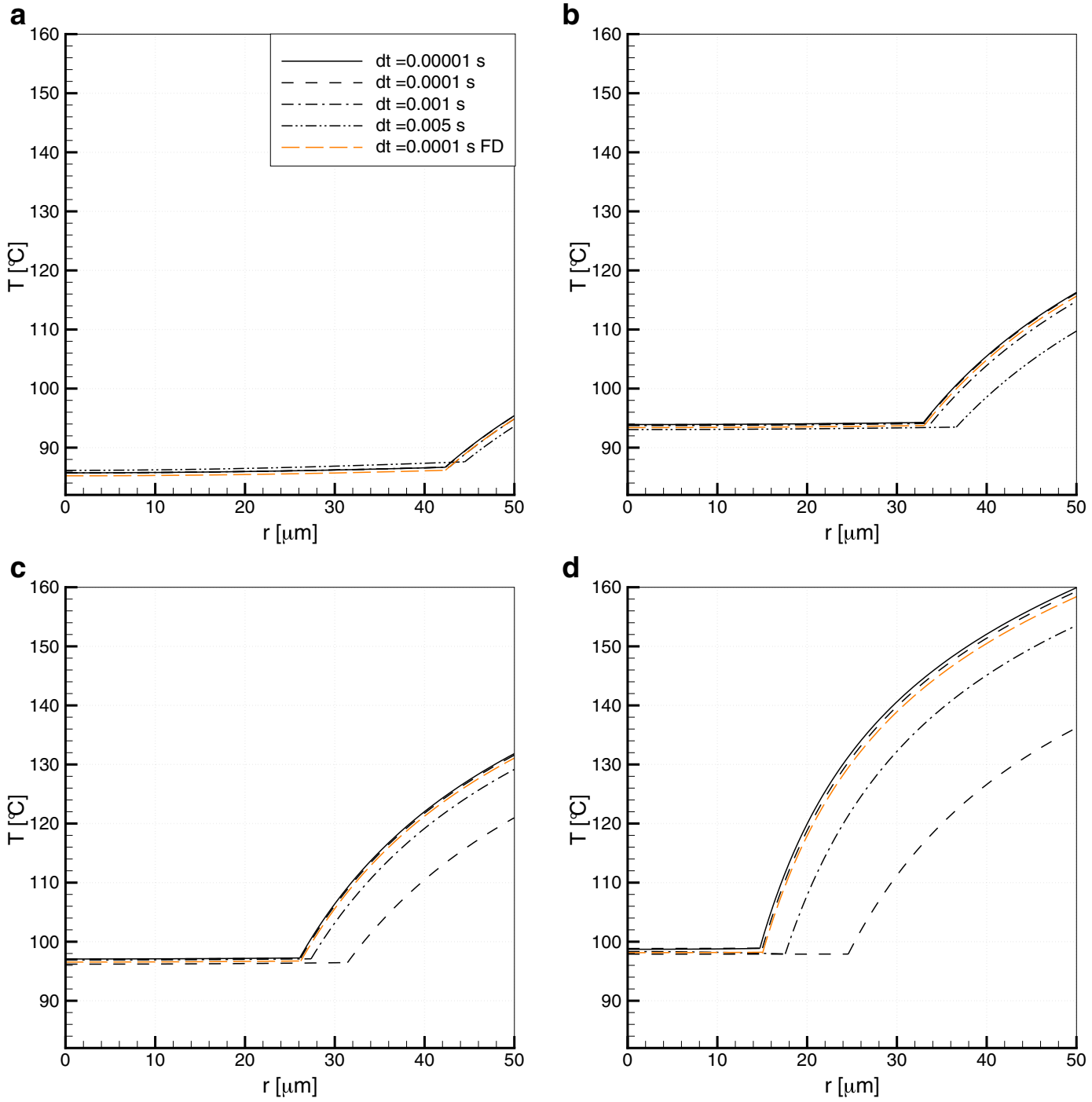

Fig. 3. Particle temperature profile through the particle drying, for different values of time steps at following times: (a) 0.03 s, (b) 0.05 s, (c) 0.06 s and (d) 0.07 s.

cussion about the drying kinetics. Results are shown in Graph, Table and Pictures forms.

5.1. Space and time discretisation

Several different calculation were made, to verified the accuracy of the numerical model. Adequacy of the mesh size and time step value were tested for particle diameter $D_p = 100$ μm and drying gas temperature $T_g = 300$ °C, which represents a fast drying kinetics, because the particle is small and air temperature high. The desired mesh element size was labelled with dx and number of computational nodes with N_n. Particles consist of a wet core and dry crust, whose sizes change through the drying process, so that the wet core size is decreased and the dry crust size is increased. At the start of the drying simulation most of the mesh elements belong to the wet core. Close to the end of the particle drying, the situation is the opposite, and most of the mesh elements belong to the dry crust. For this reason, for every time step, a new mesh has to be generated, with different numbers of mesh elements in the wet core and dry crust. Along the remeshing the values of the field functions at each node were interpolated from the old nodes positions to the new ones. At first we vary element size by keeping the time step size constant. Four different mesh element sizes were tested; $dx = 10$ μm, 2 μm, 0.5 μm and 0.2 μm, which corresponds to the number of computational nodes $N_n = 11$, 51, 201 and 501, respectively. To generate computa-

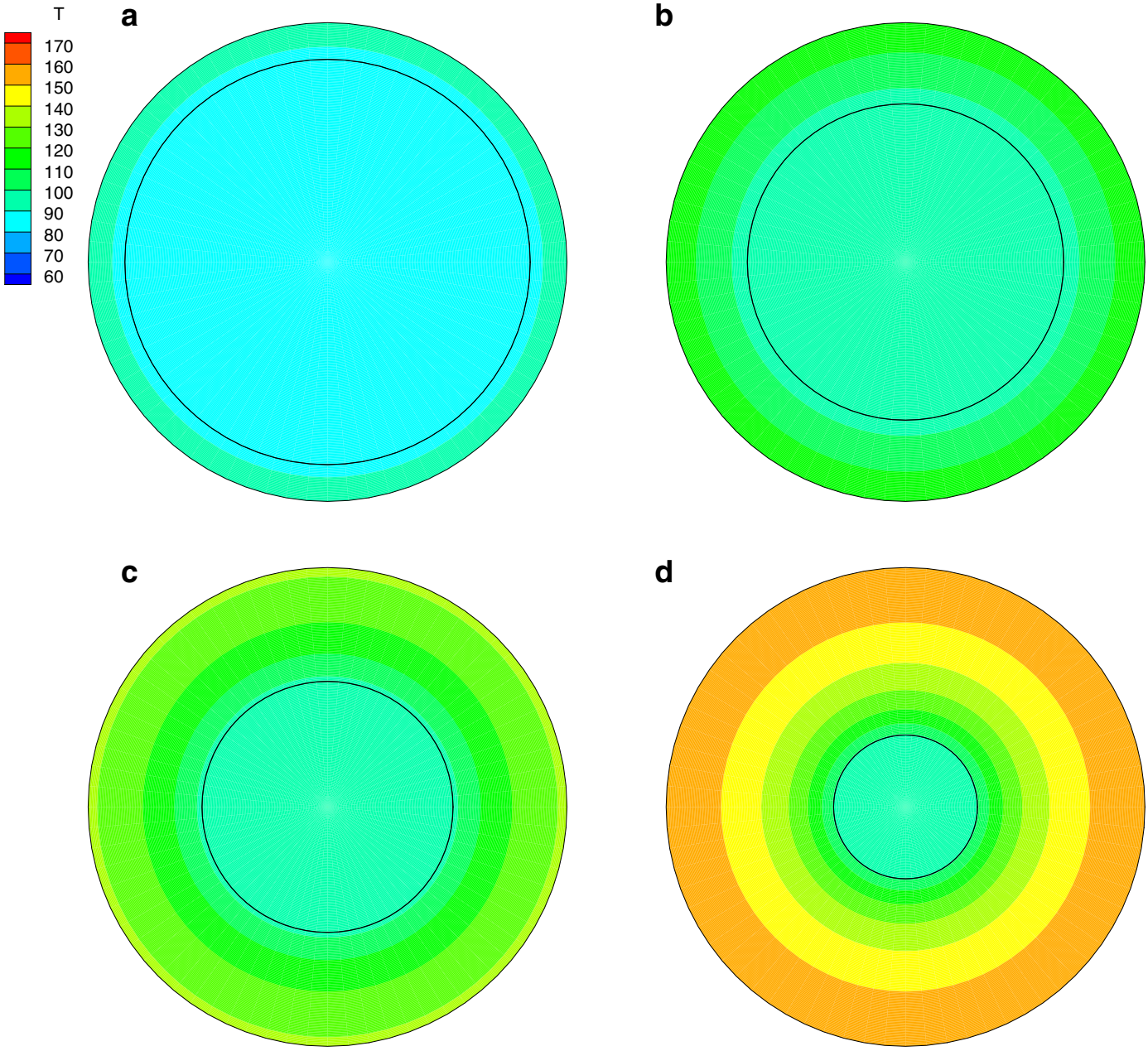

Fig. 4. Particle temperature for particle size 100 μm and drying gas temperature 300 °C at (a) drying time 0.03 s, (b) drying time 0.05 s, (c) drying time 0.06 s, (d) drying time 0.07 s.

tional mesh a structured 1D mesh in the radial direction has been used. If the mesh region (wet or dry core) was smaller than the desired mesh element size, then two quadratic mesh elements or five computational nodes were used. Particle temperature profile was compared at four different times along the drying process: $t = 0.03$ s, 0.05 s, 0.06 s and 0.07 s. Results are presented in Fig. 2, where the adequacy of two different mesh element sizes is seen. The biggest deviation between the results are present when using coarse mesh with element size of 10 μm and 11 computational nodes. When element size of 2 μm is used the numerical accuracy is better, however it still deviates slightly from the results using mesh size 0.5 μm and 0.2 μm. Identical results were obtained using mesh sizes of 0.5 μm and 0.2 μm, which were then taken as the numerically accurate results to which other results were compared.

The adequacy of the selected time step value was tested next. Four different time steps were used, and results are presented in Fig. 3 showing the particle temperature profile at four different times through the process of particle drying. In all calculations the mesh element size was set to $dx = 0.5$ μm leading to 201 computational nodes. Because the drying kinetics is fast, the drying process inside the particle proceeds very quickly, and large time steps are not suitable. Selected time steps $5 \cdot 10^{-3} s$ and $1 \cdot 10^{-3} s$ are not suitable to use, because the results deviated to much. Time steps $1 \cdot 10^{-4}$s and $1 \cdot 10^{-5}$s are suitable for use, as results comparison in Table 2 shows a low deviation. In order to lower numerical calculation costs, which, by using the time step $1 \cdot 10^{-5}$s are higher than in the case when time step $1 \cdot 10^{-4}$s is used, the latter value was our choice.

We repeated the same analysis also for the test example with the particle size $D_p = 300$ μm and the drying gas temperature $T_g = 300$ °C, where the same number of nodes has been used. Results gathered in Table 3 show, that using 201 computational nodes provide accurate numerical results, because numerical computational error compared to the finest space and time discretisation was only 0.14%. Regarding the time

Table 2
Drying time through the second drying stage for various time step values and mesh sizes together with relative error compared to the finest mesh discretisation of the particle size 100 μm and drying gas temperature 300 °C.

	dt [s]				Error [%]			
N_n	$5 \cdot 10^{-3}$	$1 \cdot 10^{-3}$	$1 \cdot 10^{-4}$	$1 \cdot 10^{-5}$	$5 \cdot 10^{-3}$	$1 \cdot 10^{-3}$	$1 \cdot 10^{-4}$	$1 \cdot 10^{-5}$
11	0.0850	0.0750	0.0728	0.0726	11.65	5.18	3.16	3.44
51	0.0850	0.0770	0.0750	0.0747	11.65	4.94	0.13	0.54
201	0.0850	0.0780	0.0753	0.0751	11.65	3.72	0.27	0.00
501	0.0850	0.0780	0.0753	0.0751	11.65	3.72	0.27	0.00

Table 3
Drying time through the second drying stage for various time steps and mesh sizes together with relative error compared to the finest discretisation for the particle size 300 μm and drying gas temperature 300 °C.

	dt (s)				Error (%)			
N_n	$5 \cdot 10^{-3}$	$1 \cdot 10^{-3}$	$1 \cdot 10^{-4}$	$1 \cdot 10^{-5}$	$5 \cdot 10^{-3}$	$1 \cdot 10^{-3}$	$1 \cdot 10^{-4}$	$1 \cdot 10^{-5}$
11	0.6	0.566	0.5638	0.5634	2.57	3.29	3.69	3.77
51	0.595	0.584	0.5811	0.5822	1.75	0.10	0.60	0.41
201	0.595	0.586	0.5838	0.5845	1.75	0.24	0.14	0.02
501	0.595	0.587	0.5844	0.5846	1.75	0.41	0.03	0.00

step value the choice of $dt = 1 \cdot 10^{-4}$s is suitable, however it can be increased when simulating a slow drying process, occuring when the drying gas temperature is low. For all the further analysis on drying kinetics a time step of $dt = 1 \cdot 10^{-4}$s and 201 computational nodes were therefore selected.

In Figs. 2 and 3 the temperature profiles inside the particle computed using a FD (Finite difference) method are shown along the BEM based results, using the same space and time discretisation as in the optimal BEM configuration. The calculation was done using Sagadin et. all [9] code with results shown with dashed orange line. It is evident that BEM based computations deliver the same accuracy of the results as the FD also when using coarser discretisations and larger time step values, clearly indicating a higher numerical accuracy of the derived BEM based computational algorithm.

5.2. Drying kinetics

Solving heat transfer problem is the basis for simulating drying process of the particle. In this section we will present drying kinetics for the particle size 100 μm which was dried with drying gas at 300 °C and analysis of how particle size, drying air temperature and particle relative velocity influence the drying time for the second stage.

Fig. 4 shows a temperature contour trough the second drying stage of the porous particle at different times. In the spray drying process, slurry droplets, usually at room temperature (25 °C), are produced by applying a pressure nozzle in the drying chamber, where it comes into contact with the hot drying air. After the first drying stage, where the surface moisture has been removed, second drying stage begins where particle interior is dried. Whenever a part of the particle interior is dried, the surface temperature increases close to the drying air temperature. A particle consists of a wet core and dry crust, which are separated by the interface where the evaporation of moisture occurs. Some heat is consumed due to the moisture evaporation at the interface. For this reason, the particle's wet core has a lower temperature than the dry crust. The black round line inside the particle presents the interface position between wet core and dry crust.

The temporal decrease of the interface radius is presented at Fig. 5(a), which, in the drying process, presents decreasing of the wet core and increasing of the dry region. When the particle interface reaches the value of zero, the particle interior is dry. The initial particle moisture content for the second drying stage of Zeolite 4*A* is 0.62 kg/kg, which decreases through the drying process, as can be seen from the Fig. 5(b).

The drying kinetics of porous particles are strongly dependent on the particle size and drying gas temperature. When the drying particles are small and drying air temperatures high, we are dealing with very fast drying kinetics, which demand the finest space and time discretisation. Fig. 6(a) shows the particle drying time depending on the particle diameter and drying gas temperature. For small particles, temperature of

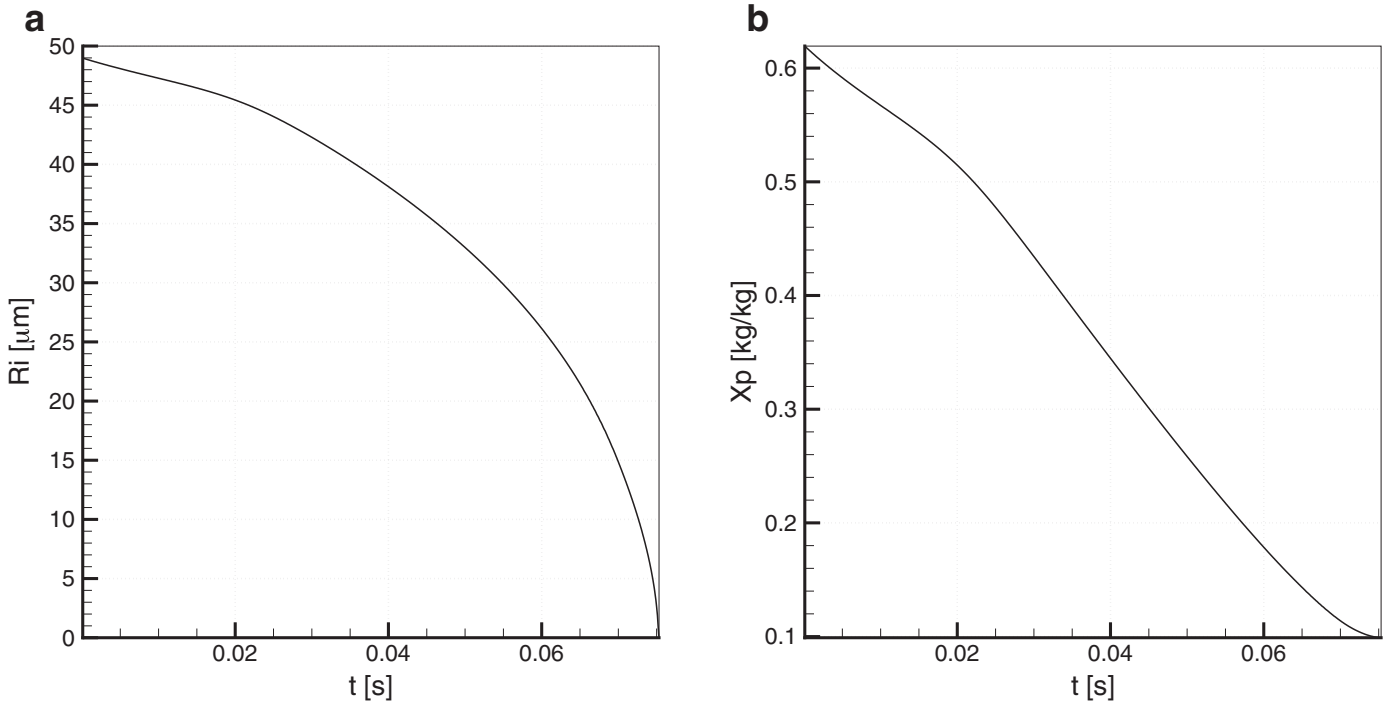

Fig. 5. Interface radius change (a) and particle absolute moisture change (b) with respect to time.

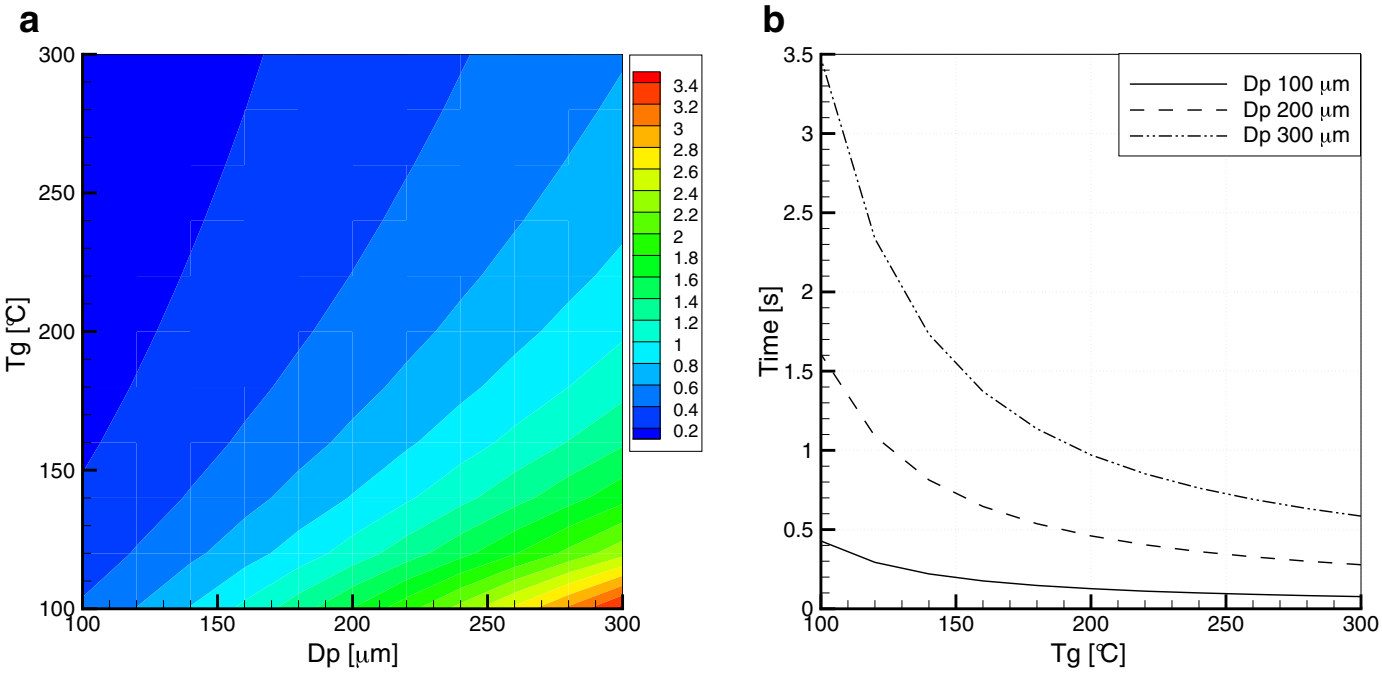

Fig. 6. Influence of particle diameter and drying gas temperature on drying time.

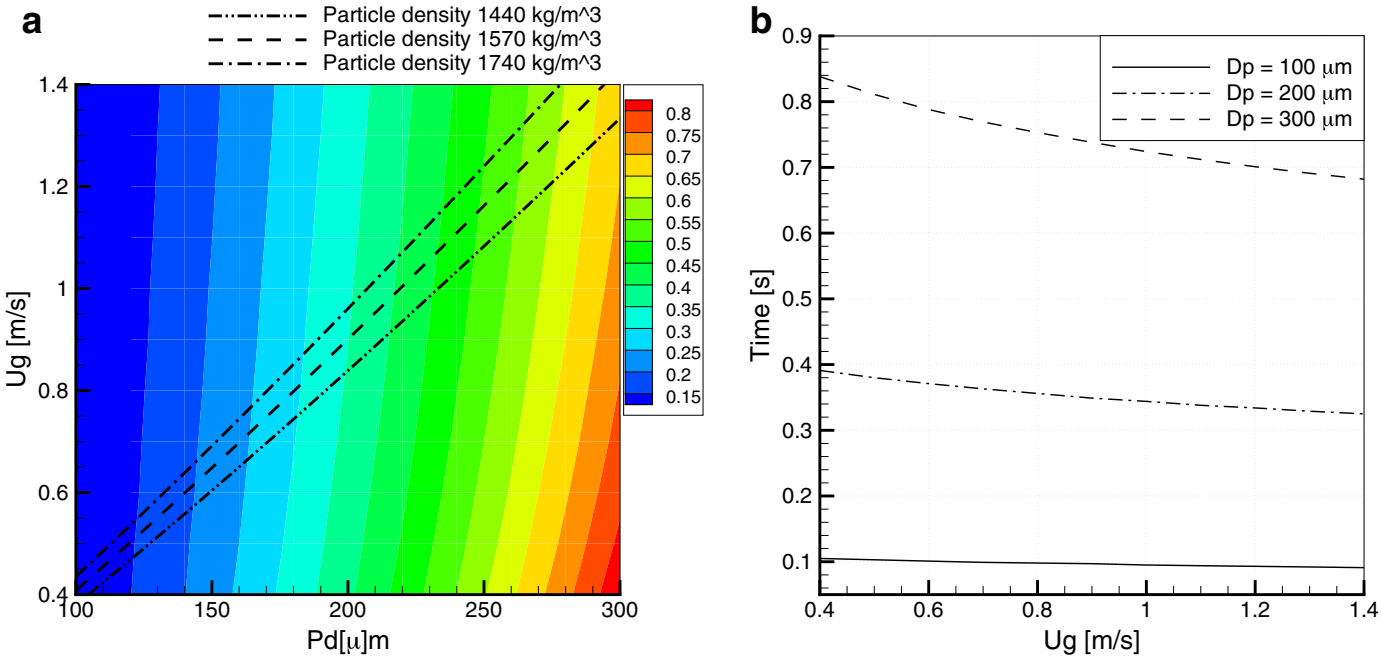

Fig. 7. Influence of particle diameter and particle relative velocity on drying time.

the drying gas do not have a great influence on the total drying time, as is the case for the bigger ones. This is especially visible from the Fig. 6 (b) showing the drying time for three different particle sizes. As can be observed, the drying gas temperature has the biggest influence on the drying time in the lower temperature range, this is between 100 °C and 150 °C.

Fig. 7 shows the effect of the relative particle velocity and the particle diameter on the drying time. As already observed form the Fig. 6 the diameter has a high impact on the drying time, however the relative velocity does not, as the change in the value o the heat transfer coefficient is not substantial. Fig. 7 (a) shows the three lines presenting the largest relative velocity between the drying gas and the particle size that can occur in the drying column for different particle density of the wet zeolite, which range between the 1440 kg/m^3 and 1740 kg/m^3. The largest relative velocity depends on the particle diameter and has been determined by equation [17]:

$$U = \sqrt[1.4]{\frac{M_p g}{\frac{1}{2}18.5\mu^{0.6} D_p^{-0.6} \rho_f^{0.4} A}}, \tag{25}$$

where M_p represents particle mass, g gravity acceleration, μ dynamic viscosity of drying gas, D_p particle diameter, ρ_f drying fluid density and $A = \pi D_p^2/4$ projected area of the particle. To conclude, Figs. 6 and 7 show the drying time for different particle size and drying conditions that can be practically used in designing the drying column, where drying gas temperature and particle size play an important role.

6. Conclusion

In this paper, a porous particle drying problem was studied using the Boundary Element Method based computational model. Although the drying of a spherical porous particle is typically divided into two or three stages, depending on if the material is hygroscopic or not, this paper investigates the numerical solution of the second drying stage, which is most relevant for the porous material. The heat transfer problem inside the spherical particle with moving drying front was solved using BEM approach. Because drying of the spherical particle under uniform boundary conditions was assumed, a 3D problem was transformed into a quasi 1D problem with the solution depending only on the radial direction. The solution of the heat transfer inside the particle is the most important aspect in accurate evaporation calculation on the interface between the dry and wet region within the particle, as it directly affects the level of vapor saturation pressure and consequently the drying time. The analysis of the space and time discretisation was done on two different test examples showing that the 201 nodes and $dt = 1 \cdot 10^{-4}$ s is sufficient to accurately simulate second drying stage even for small droplets and high drying times. An extensive analysis showed how the particle diameter, the drying gas temperature and the relative velocity affect the drying time, with the particle size and drying temperature being the most important ones. From this study the drying time of the second stage for the Zeolite 4*A*water droplet was evaluated under conditions found in drying column design. In the future work, the elliptic fundamental solution will be replaced by the parabolic fundamental solution, which will allow an elimination of the domain integral, which is now solved using numerical integration and represents the computationally most demanding part.

Acknowledgments

The authors wish to thank the Slovenian Research Agency (ARRS) for the financial support in the framework of the programme P2-0196 Research in Power, Process, and Environmental Engineering.

References

[1] Fu N, Woo MW, Lin SXQ, Zhou Z, Chen XD. Reaction engineering approach (REA) to model the drying kinetics of droplets with different initial sizes-experiments and analyses. Chem Eng Sci 2011;66(8):1738–47.
[2] Langrish T, Kockel T. The assessment of a characteristic drying curve for milk powder for use in computational fluid dynamics modelling. Chem Eng J 2001;84(1):69–74.
[3] Levi-Hevroni D, Levy A, Borde I. Mathematical modeling of drying of liquid/solid slurries in steady state one-dimensional flow. Dry Technol 1995;13(5–7):1187–201.
[4] Shampine LF. Numerical solution of ordinary differential equations. Routledge; 2018.
[5] Mezhericher M, Levy A, Borde I. Theoretical drying model of single droplets containing insoluble or dissolved solids. Dry Technol 2007;25(6):1025–32.
[6] Mezhericher M, Levy A, Borde I. Heat and mass transfer of single droplet/wet particle drying. Chem Eng Sci 2008;63(1):12–23.
[7] Handscomb C, Kraft M, Bayly A. A new model for the drying of droplets containing suspended solids after shell formation. Chem Eng Sci 2009;64(2):228–46.
[8] Sagadin G, Hriberšek M, Škerget L. Multiphase numerical model of spray drying of zeolite-water suspension. Comput Methods Therm Probl 2014;14:481.
[9] Sagadin G, Hriberšek M. A multistage spray drying model for zeolite 4a–water suspensions in a counter-current spray dryer. Int J Heat Mass Transf 2017;108:1220–8.
[10] Langrish T. Multi-scale mathematical modelling of spray dryers. J Food Eng 2009;93(2):218–28.
[11] Ravnik J, Hribersek M, Vogel F, Steinmann P. Numerical simulation of particle movement in cellular flows under the influence of magnetic forces. Int J Simul Model 2014;13(3):300–12.
[12] Ravnik J, Škerget L, Hriberšek M, Žunič Z. Numerical simulation of dilute particle laden flows by wavelet BEM–FEM. Comput Methods Appl Mech Eng 2008;197(6–8):789–805.
[13] Fletcher D, Guo B, Harvie D, Langrish T, Nijdam J, Williams J. What is important in the simulation of spray dryer performance and how do current CFD models perform? Appl Math Model 2006;30(11):1281–92.
[14] Ramšak M, Škerget L. A highly efficient multidomain BEM for multimillion subdomains. Eng Anal Bound Elem 2014;43:76–85.
[15] Iljaž J, Wrobel L, Hriberšek M, Marn J. Subdomain BEM formulations for the solution of bio-heat problems in biological tissue with melanoma lesions. Eng Anal Bound Elem 2017;83:25–42.
[16] Ramšak M, Ravnik J, Zadravec M, Hriberšek M, Iljaž J. Freeze-drying modeling of vial using BEM. Eng Anal Bound Elem 2017;77:145–56.
[17] Clark MM. Transport modeling for environmental engineers and scientists, 1991. Wiley Online Library; 1996.